The Astrophysical Journal, 940:21 (7pp), 2022 November 20 https://doi.org/10.3847/1538-4357/ac958d

Change of Rankine–Hugoniot Relations during Postshock Relaxation of Anisotropic Distributions

Michael Gedalin[1], Michal Golan[1], Nikolai V. Pogorelov[2,3], and Vadim Roytershteyn[4]
[1] Department of Physics, Ben Gurion University of the Negev, Beer-Sheva, Israel; gedalin@bgu.ac.il
[2] Department of Space Science, The University of Alabama in Huntsville, AL 35805, USA
[3] Center for Space Plasma and Aeronomic Research, The University of Alabama in Huntsville, AL 35805, USA
[4] Space Science Institute, Boulder, CO 80301, USA
Received 2022 July 20; revised 2022 September 25; accepted 2022 September 26; published 2022 November 16

Abstract

Collisionless shocks channel the energy of the directed plasma flow into the heating of the plasma species and magnetic field enhancement. The kinetic processes at the shock transition cause the ion distributions just behind the shock to be nongyrotropic. Gyrotropization and subsequent isotropization occur at different spatial scales. Accordingly, for a given upstream plasma and magnetic field state, there would be different downstream states corresponding to the anisotropic and isotropic regions. Thus, at least two sets of Rankine–Hugoniot relations are needed, in general, to describe the connection of the downstream measurable parameters to the upstream ones. We establish the relation between the two sets.

Unified Astronomy Thesaurus concepts: Shocks (2086); Interplanetary shocks (829); Planetary bow shocks (1246)

1. Introduction

Collisionless shocks are one of the most fundamental nonlinear phenomena in space plasmas. Shocks have been a focus of research for more than half a century (de Hoffmann & Teller 1950; Sagdeev 1966), mainly because of their efficiency in charged particle acceleration. A collisionless shock is a multiscale object. Leaving aside the smallest scale, related to electron heating (Feldman et al. 1982; Thomsen et al. 1985; Tokar et al. 1986; Thomsen et al. 1987; Schwartz et al. 1988; Balikhin et al. 1993; Balikhin & Gedalin 1994; Krasnosselskikh et al. 1995; Savoini et al. 2005; Schwartz et al. 2011), and the largest scale of diffusive shock acceleration (Jokipii 1966; Sonnerup 1969; Axford et al. 1977; Krymskii 1977; Bell 1978; Toptyghin 1980; Blandford & Eichler 1987; Jones 1994; Giacalone 2003; Vink 2004; Jokipii et al. 2007), there are still at least three ion-related scales. At the scale of the shock transition itself, the electric and magnetic fields of the shock convert the presumably isotropic incident (upstream) ion distribution into a nongyrotropic distribution in the downstream region just behind the transition (Sckopke et al. 1983, 1990; Gedalin & Zilbersher 1995; Li et al. 1995; Gedalin 1997). Further into the downstream, gyrophase mixing produces a gyrotropic but anisotropic distribution (Sckopke et al. 1983, 1990; Gedalin 2015; Gedalin et al. 2015; Gedalin 2019a, 2019b). Further on, interaction with fluctuating fields results in isotropization. At each scale, the plasma state and the corresponding magnetic field are determined by the upstream plasma and magnetic field parameters, but in different ways. At the isotropic, magnetohydrodynamic (MHD), scale, the upstream and downstream states are assumed to be time-independent and uniform, while the shock itself is treated as a discontinuity. The two states are then related by the Rankine–Hugoniot relations (RH), which are nothing but the conservation laws and the requirement of continuity of the tangential component of the electric field (de Hoffmann & Teller 1950; Kennel 1988; Gedalin 2017). One of the important elements of the conservation laws is the equation of state of the plasma, i.e., the relation of the internal energy density and the pressure. At the gyrotropic scale, the upstream and downstream states can still be assumed to be time-independent and uniform, and the relation between them can still be described by conservation laws, only the equation of state is different. Thus, another set of RH is needed (Abraham-Shrauner 1967; Lynn 1967; Hudson 1970; Lyu & Kan 1986; Génot 2009; Gedalin et al. 2020, 2021). In what follows, we shall refer to the MHD Rankine–Hugoniot relations as mRH, and to the Rankine–Hugoniot relations on the anisotropic gyrotropic scale as aRH. The application of the conservation laws at the nongyrotropic scale, comparable to the width of the shock transition, leads to another set of RH (Gedalin & Balikhin 2008; Gedalin 2021). It is well known that the downstream pressures obtained with mRH and aRH are different (Erkaev et al. 2000; Vogl et al. 2001; Génot 2009), although little attention has been paid to different magnetic compressions. However, magnetic field measurements are the most reliable measurements at shocks. In a turbulent shock, the transition from nongyrotropy to isotropy may be short, so that only mRH make sense when comparing measurements of the plasma in the upstream and downstream regions. In laminar or less turbulent shocks, the length of the region over which isotropization occurs may be large. In such shocks, the measured plasma state depends on the temporal resolution and/or time of accumulation of the instrument. As an example, the Ulysses instrument SWOOPS provides data accumulated over hours (Bame et al. 1992), while a shock is crossed within tens of seconds. During the isotropization process, the plasma parameters and magnetic field evolve from those determined by aRH to those satisfying mRH. It is important to know how they are related.

2. The Anisotropy of the Downstream Ion Temperature: An Observational Example

We illustrate the anisotropy of the downstream ion distributions behind the shock front using a Magnetospheric

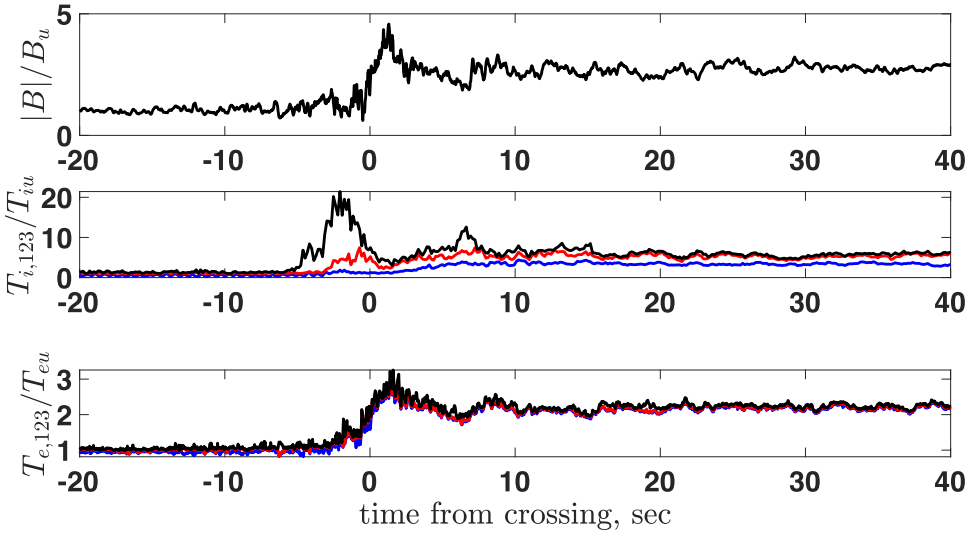

Figure 1. Top: the magnetic field magnitude, normalized to the upstream magnetic field magnitude. Middle: the three eigenvalues of the ion temperature tensor, normalized to the upstream ion temperature. Bottom: the three eigenvalues of the electron temperature tensor, normalized to the upstream electron temperature. The smallest eigenvalue is in blue, while the largest one is in black. The measurements are conducted in burst mode. See the text for more details.

MultiScale (MMS) observed shock as an example. The bow shock crossing on 2011 November 2 at 04:26:42, observed by MMS3, is described by Hanson et al. (2019). In what follows, we use the measurements of MMS4 at the same shock. Figure 1 shows the magnetic field and the eigenvalues of the temperature tensor for this shock. The magnetic field is provided by the FluxGate Magnetometer instrument in burst mode (128 samples per second; Russell et al. 2016). The ion and electron moments are provided by the Fast Plasma Investigation (FPI) instrument in burst mode (once per 150 ms for ions and per 30 ms for electrons; Pollock et al. 2016). FPI provides the total temperature tensor, which can be diagonalized without the determination of the shock normal or the shock Mach number. The upper panel shows the magnetic field profile with all the typical attributes of a supercritical shock with substantial ion reflection: the foot, the ramp, the overshoot, and the undershoot. The middle panels show that the strongest ion heating occurs in the foot, where the strongest anisotropy is also observed. The downstream ion temperature is substantially lower than in the foot. The temperature is the measure of the velocity dispersion, and the high temperature in the foot is due to the counterstreaming populations of the incident and reflected ions. Anisotropy persists well behind the shock transition. Weak anisotropy appears in the measurements upstream of the shock. Most probably, this is an instrumental effect, due to the difficulties of accurately measuring the cold solar wind. The electron temperature is almost isotropic and the heating follows the magnetic field. Figure 2 shows the parallel (blue) and perpendicular (black) temperatures of ions normalized to the upstream ion temperature measured by FPI in the fast mode, once per 4.5 s. The anisotropy of $T_\parallel/T_\perp \approx 0.8$ persists well beyond the shock front. Figure 3 shows that the ratio $T_{\max}/T_{\min} > 1$ is measured far downstream of the shock transition. Nevertheless, it is expected that, sufficiently far from the shock, the downstream parallel and perpendicular temperatures will equalize.

3. Conservation Laws

A plasma consists of a number of species, denoted by the index s, each of which has its own distribution function $f_s(\boldsymbol{v})$. In the present paper, we limit ourselves to nonrelativistic velocities only. The moments of the distribution function give the number density n_s and the mass density ρ_s,

$$n_s = \int f_s(\boldsymbol{v})d\boldsymbol{v}, \quad \rho_s = m_s n_s, \tag{1}$$

the hydrodynamical velocity $\boldsymbol{U}_s$,

$$n_s \boldsymbol{U}_s = \int \boldsymbol{v} f_s(\boldsymbol{v})d\boldsymbol{v}, \tag{2}$$

the pressure tensor,

$$p_{s,ij} = m_s \int (v_i - U_{s,i})(v_j - U_{s,j}) f_s(\boldsymbol{v})d\boldsymbol{v}, \tag{3}$$

and the energy density,

$$\epsilon_s = \frac{1}{2} m_s \int (\boldsymbol{v} - \boldsymbol{U}_s)^2 f_s(\boldsymbol{v})d\boldsymbol{v} = \frac{1}{2}\sum_i p_{ii}, \tag{4}$$

where m_s is the mass of a particle of the species s and $i, j = x, y, z$. In what follows, we consider only the distributions for which the heat flux vanishes identically:

$$\int (v_i - U_{s,i})(v_j - U_{s,j})(v_k - U_{s,k}) f_s(\boldsymbol{v})d\boldsymbol{v} = 0. \tag{5}$$

In order to proceed, we introduce the following notation: the indices u and d denote the uniform upstream and downstream regions, respectively. If an expression does not contain any of these indices, it is valid for each one of the uniform regions. The shock normal is chosen in the x-direction, and the coplanarity plane is the $x - z$-plane. The uniform magnetic field is $\boldsymbol{B} = (B_x, 0, B_z)$, and the angle between this magnetic field and the shock normal is θ. In what follows, we adopt the assumption that in the upstream and downstream regions, the hydrodynamical velocities of all species are equal:

$$\boldsymbol{U}_{s,u} = \boldsymbol{U}_u, \quad \boldsymbol{U}_{s,d} = \boldsymbol{U}_d. \tag{6}$$

In this case, the density, pressure, and energy density used in the conservation laws are obtained by summation over the

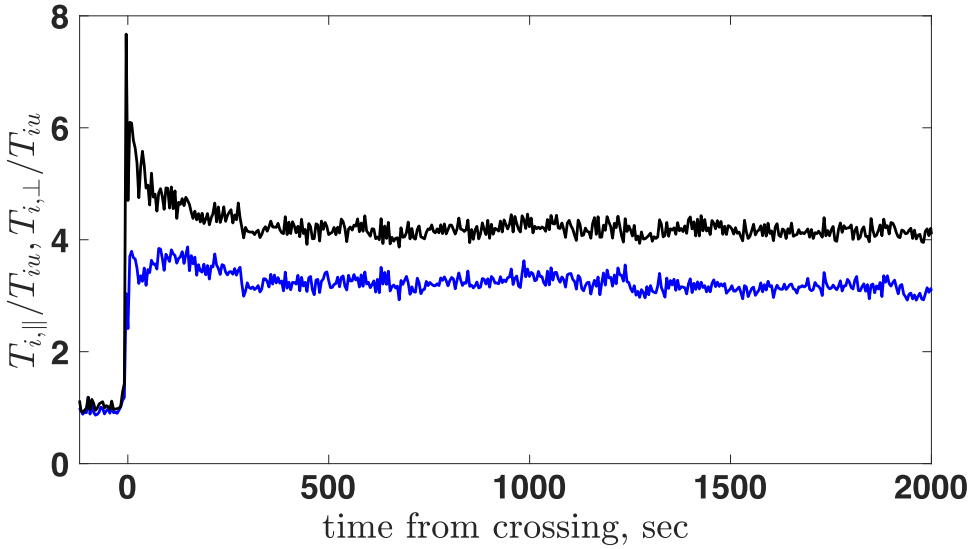

Figure 2. The parallel (blue) and perpendicular (black) temperatures of ions normalized to the upstream ion temperature.

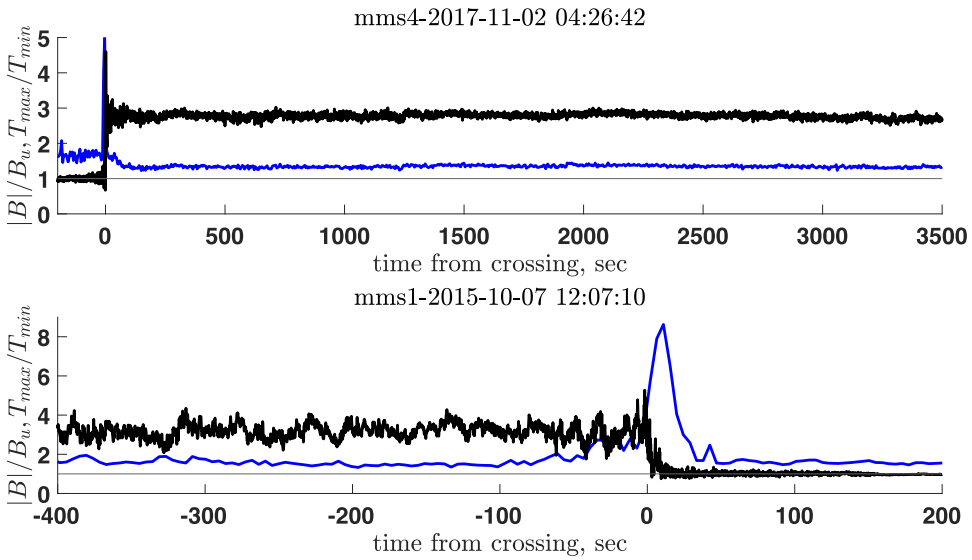

Figure 3. The normalized magnetic field magnitude $|B|/B_u$ (black) and the ratio of the largest to smallest eigenvalues of the temperature tensor $T_{\max}/T_{\min}$ (blue) for two MMS-observed shocks. The thin black line corresponds to $T_{\max}/T_{\min} = 1$.

species:

$$\rho = \sum_s \rho_s, \quad p_{ij} = \sum_s p_{s,ij}, \quad \epsilon = \sum_s \epsilon_s. \tag{7}$$

The conservations of mass, momentum, and energy require that the mass density flux J_i, the momentum density flux P_{ij}, and the energy density flux Q_i be equal on both sides of the shock. All fluxes will be written in the de Hoffman–Teller frame (HT; de Hoffmann & Teller 1950). In the HT, the velocity $\boldsymbol{U} = U(\cos\theta, 0, \sin\theta)$ is along the magnetic field $\boldsymbol{B} = B(\cos\theta, 0, \sin\theta)$, and the electric field vanishes, both upstream and downstream. Accordingly, the energy density flux does not include the Poynting flux:

$$J_i = \rho U_i, \tag{8}$$

$$P_{ij} = \rho U_i U_j + p_{ij} + \frac{B^2}{8\pi}\delta_{ij} - \frac{B_i B_j}{4\pi}, \tag{9}$$

$$Q_i = \left(\frac{1}{2}\rho U^2 + \epsilon\right)U_i + \sum_j p_{ij} U_j, \tag{10}$$

where δ_{ij} is the Kronecker tensor. Since the pressure and energy density are defined via the velocity dispersion in the fluid frame, they are the same in the HT and in the normal incidence frame (where the upstream plasma flow is along the shock normal), provided that the transformation between the two frames is nonrelativistic, $U_u \ll c$. Here, c is the light speed. We are interested in the plasma state in the regions where the pressure is gyrotropic but possibly anisotropic:

$$p_{ij} = p_\| b_i b_j + p_\perp(\delta_{ij} - b_i b_j) = p_\perp(\delta_{ij} + (A-1)b_i b_j), \tag{11}$$

$$\epsilon = p_\perp + \frac{1}{2}p_\| = \left(1 + \frac{A}{2}\right)p_\perp, \tag{12}$$

where $b_i = B_i/B$ and $A = p_\|/p_\perp$ is the anisotropy ratio. In what follows, we assume that the upstream pressure is isotropic.

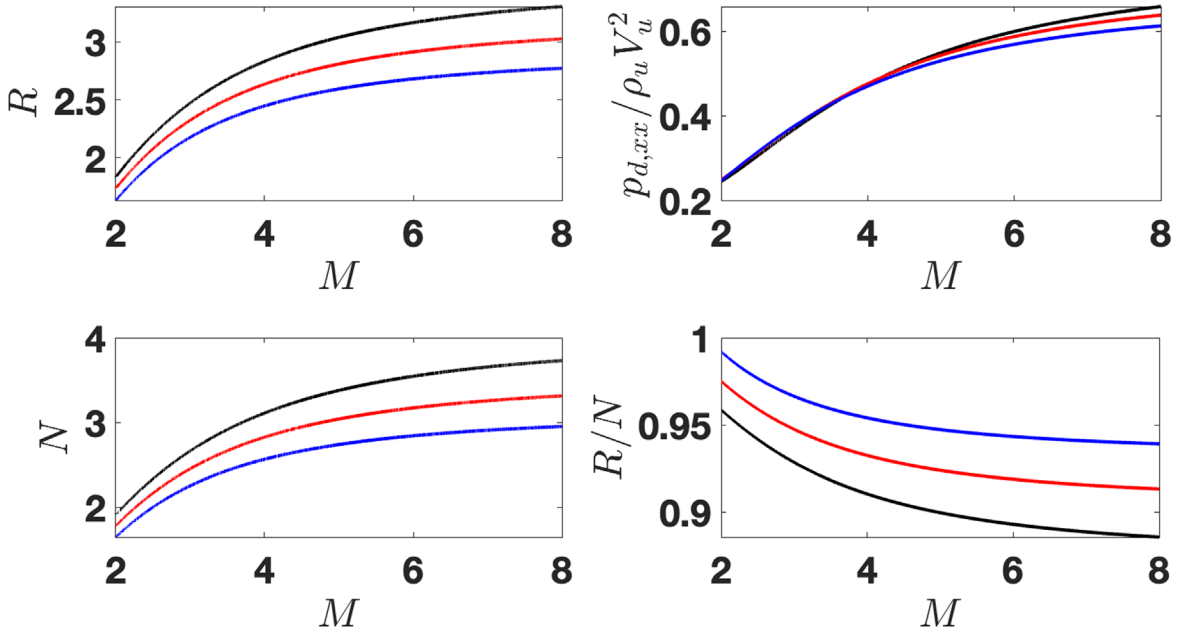

Figure 4. Various parameters as functions of the Alfvénic Mach number M for $A = 1$ (black curves), $A = 0.5$ (red curves), and $A = 0.1$ (blue curves). Top left: the magnetic compression $R = B_d/B_u$. Top right: the normalized downstream pressure $\Pi_{xx} = p_{d,xx}/\rho_u V_u^2$. Bottom left: the density compression $N = n_d/n_u$. Bottom right: the ratio of the magnetic compression to the density compression R/N . The shock angle is $\theta_u = 60°$ and $\beta = 0.5$.

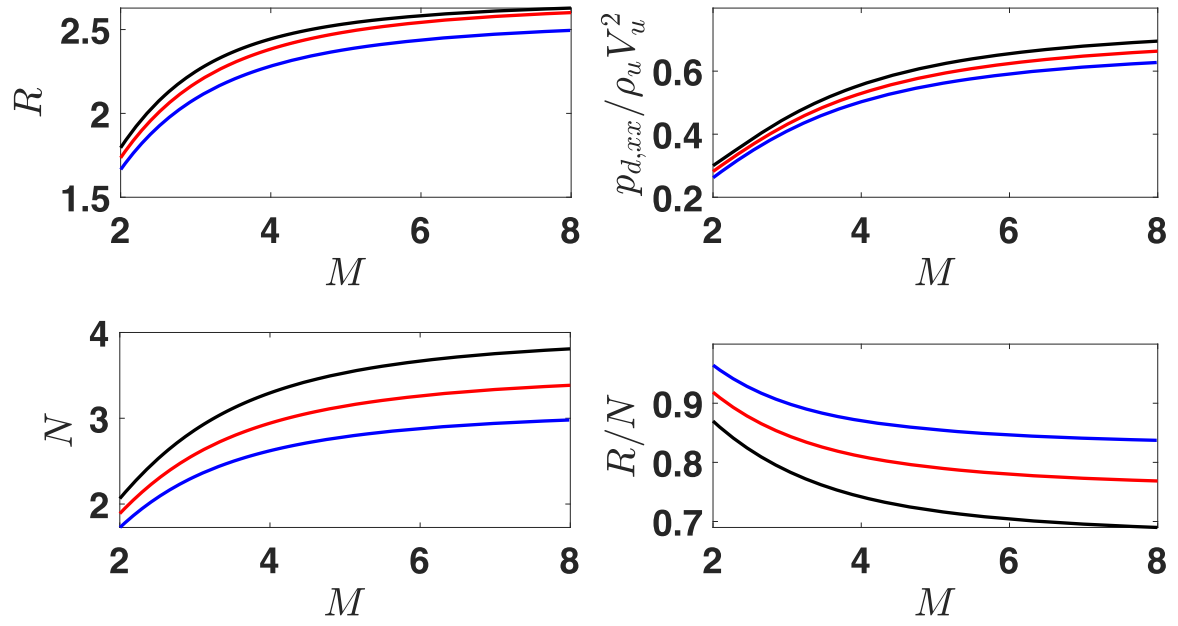

Figure 5. Various parameters as functions of the Alfvénic Mach number M for $A = 1$ (black curves), $A = 0.5$ (red curves), and $A = 0.1$ (blue curves). Top left: the magnetic compression $R = B_d/B_u$. Top right: the normalized downstream pressure $\Pi_{xx} = p_{d,xx}/\rho_u V_u^2$. Bottom left: the density compression $N = n_d/n_u$. Bottom right: the ratio of the magnetic compression to the density compression R/N. The shock angle is $\theta_u = 40°$ and $\beta = 0.5$.

Different species are heated differently upon the shock crossing. In a plasma consisting mainly of thermal protons and electrons, with only a small addition of superthermal particles (like pickup ions) or heavy species, the downstream pressure is dominated by protons. Unless the shock is nearly parallel, the proton heating is mainly in the direction perpendicular to the magnetic field, thus causing strong anisotropy at the shock transition. This anisotropy relaxes farther downstream. It has been suggested that the downstream anisotropy is determined by the threshold of the mirror instability (Erkaev et al. 2000; Vogl et al. 2001). However, mirror-mode structures have been observed in the Earth magnetosheath even for supposedly stable conditions (Balikhin et al. 2010). Therefore, in the present study, we do not relate the anisotropy ratio to any instability, but leave it as a free parameter. Previous studies (Erkaev et al. 2000; Vogl et al. 2001, 2003; Génot 2009) have concentrated on the anisotropic plasma parameters in the downstream region. We are mostly interested in the difference in the magnetic compression that would be observed in the isotropic and anisotropic regimes for the same upstream conditions. For the chosen shock coordinates above, the

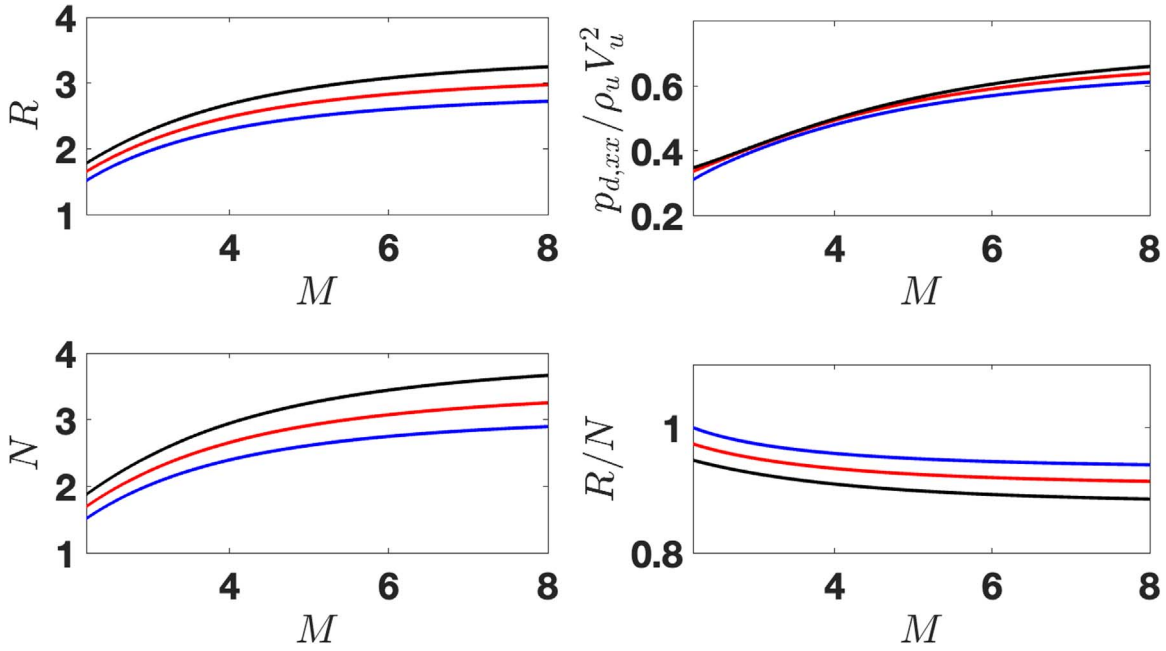

Figure 6. Various parameters as functions of the Alfvénic Mach number M for $A = 1$ (black curves), $A = 0.5$ (red curves), and $A = 0.1$ (blue curves). Top left: the magnetic compression $R = B_d/B_u$. Top right: the normalized downstream pressure $\Pi_{xx} = p_{d,xx}/\rho_u V_u^2$. Bottom left: the density compression $N = n_d/n_u$. Bottom right: the ratio of the magnetic compression to the density compression R/N. The shock angle is $\theta_u = 60°$ and $\beta = 1$.

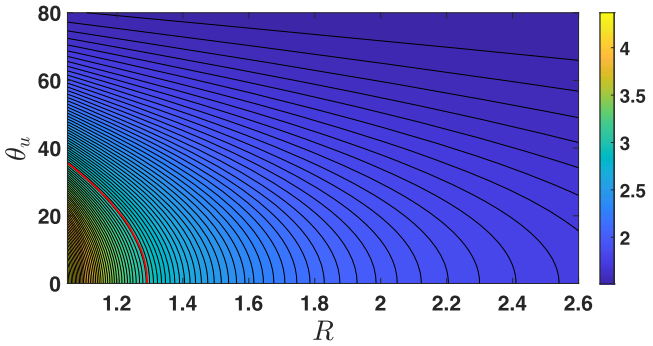

Figure 7. The number of DOF ν as a function of B_d/B_u and θ_u.

conserved fluxes are

$$J_x = \rho U \cos\theta, \tag{13}$$

$$P_{xx} = \rho U^2 \cos^2\theta + p_\perp \sin^2\theta + p_\parallel \cos^2\theta + \frac{B^2}{8\pi} - \frac{B^2\cos^2\theta}{4\pi}, \tag{14}$$

$$P_{zx} = P_{xz} = \rho U^2 \cos\theta \sin\theta + (p_\parallel - p_\perp) \times \cos\theta \sin\theta - \frac{B^2 \cos\theta \sin\theta}{4\pi}, \tag{15}$$

$$Q_x = \left(\frac{1}{2}\rho U^2 + \epsilon + p_\parallel\right) U \cos\theta, \tag{16}$$

which, together with $B_x = B_u \cos\theta_u = B_d \cos\theta_d = \text{const}$, $p_{d,\parallel} = A p_{d,\perp}$, and $p_{u,\perp} = p_{u,\parallel} = p_u$, give

$$B_u \cos\theta_u = B_d \cos\theta_d, \tag{17}$$

$$\rho_u U_u \cos\theta_u = \rho_d U_d \cos\theta_d, \tag{18}$$

$$\rho_u U_u^2 \cos^2\theta_u + p_u + \frac{B_u^2}{8\pi} = \rho_d U_d^2 \cos^2\theta_d + p_{d,\perp}(1 + (A-1)\cos^2\theta_d) + \frac{B_d^2}{8\pi}, \tag{19}$$

$$\rho_u U_u^2 \cos\theta_u \sin\theta_u - \frac{B_u^2 \cos\theta_u \sin\theta_u}{4\pi} = \rho_d U_d^2 \cos\theta_d \sin\theta_d + p_{d,\perp}(A-1)\cos\theta_d \sin\theta_d - \frac{B_d^2 \cos\theta_d \sin\theta_d}{4\pi}, \tag{20}$$

$$\left(\frac{1}{2}\rho_u U_u^2 + \frac{5}{2}p_u\right) U_u \cos\theta_u = \left(\frac{1}{2}\rho_d U_d^2 + \left(1 + \frac{3A}{2}\right)p_{d,\perp}\right) U_d \cos\theta_d. \tag{21}$$

We switch to normalized variables:

$$R = \frac{B_d}{B_u} = \frac{\cos\theta_u}{\cos\theta_d}, \quad N = \frac{\rho_d}{\rho_d}, \quad Y = \frac{U_d}{U_u}, \quad \Pi = \frac{p_{d,\perp}}{\rho_u U_u^2 \cos^2\theta_u}. \tag{22}$$

Here, R is the magnetic compression and N is the density compression. The Alfvén speed is $v_A = B_u/\sqrt{4\pi\rho_u}$ and the Alfvénic Mach number is $M = V_u/v_A$, where $V_u = U_u \cos\theta_u$ is the upstream flow velocity along the shock normal, i.e., the shock speed. We also define, as usual, $\beta = 8\pi p_u/B_u^2$. Now, using the above normalization and the physical variables, we get the conservations laws, aka RH, in the form

$$NY = R, \tag{23}$$

$$1 + \frac{\beta+1}{2M^2} = \frac{Y}{R} + \Pi\left(1 + (A-1)\frac{\cos^2\theta_u}{R^2}\right) + \frac{R^2}{2M^2}, \tag{24}$$

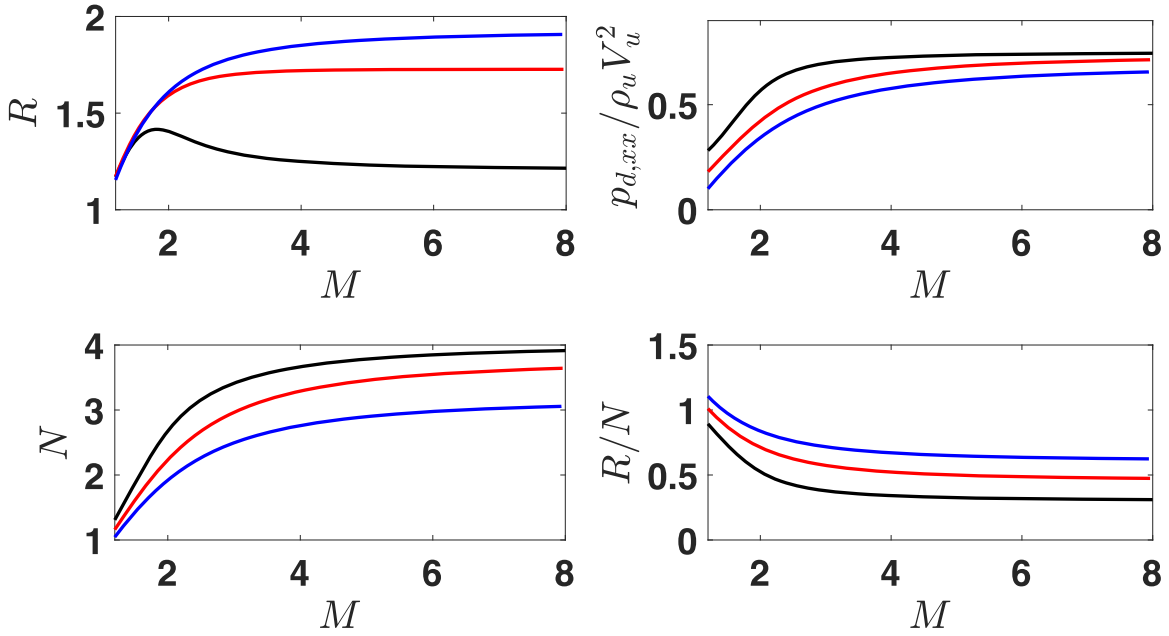

Figure 8. Various parameters as functions of the Alfvénic Mach number M for $A = 1$ (black curves), $A = 0.5$ (red curves), and $A = 0$ (blue curves). Top left: the magnetic compression $R = B_d/B_u$. Top right: the normalized downstream pressure $\Pi_{xx} = p_{d,xx}/\rho_u V_u^2$. Bottom left: the density compression $N = n_d/n_u$. Bottom right: the ratio of the magnetic compression to the density compression R/N. The shock angle is $\theta_u = 10°$ and $\beta = 0.5$.

$$1 - \frac{\cos^2\theta_u}{M^2} = \left(Y - \frac{R\cos^2\theta_u}{M^2} + \frac{\Pi\cos^2\theta_u(A-1)}{R}\right)\left(\frac{\sin\theta_d}{\sin\theta_u}\right), \tag{25}$$

$$\frac{1}{2} + \frac{5\beta\cos^2\theta_u}{4M^2} = \frac{Y^2}{2} + \left(\frac{\Pi Y}{R}\right)\left(1 + \frac{3A}{2}\right)\cos^2\theta_u, \tag{26}$$

where $\sin\theta_d = \sqrt{1 - \cos^2\theta_u/R^2}$.

Figures 4 and 5 show the dependencies of various parameters on the Alfvénic Mach number for $A = 1$ (black curves), $A = 0.5$ (red curves), and $A = 0.1$ (blue curves). The shown parameters are the magnetic compression $R = B_d/B_u$ (top left), the density compression $N = n_d/n_u$ (bottom left), the normalized downstream pressure $\Pi_{xx} = p_{d,xx}/\rho_u V_u^2$ (top right), and the ratio of the magnetic compression to the density compression R/N (bottom right). Two shock angles are shown, $\theta_u = 60°$ and $\theta_u = 40°$. In both cases, $\beta = 0.5$, which is rather typical for the Earth bow shock (Farris et al. 1993). The downstream plasma pressure $p_{d,xx}$ is not sensitive to the anisotropy A, while the downstream energy density ϵ_d is substantially lower in the anisotropic case, which is accompanied by a lower density compression ratio. The latter means that the total downstream pressure P_{xx} and, therefore, the downstream magnetic pressure, are lower in the anisotropic case.

Figure 6 shows the dependencies of various parameters on the Alfvénic Mach number in the same format as Figure 4, but for $\beta = 1$. The behavior is similar.

Anisotropy effectively reduces the number of degrees of freedom (DOF) ν:

$$n = \frac{3A + 2}{1 + (A-1)\cos^2\theta_d} - 2. \tag{27}$$

Figure 7 shows that the effective number of DOF is lower in the anisotropic case, except for low magnetic compressions in nearly parallel shocks. The red curve separates the regions $\nu < 3$ and $\nu > 3$. In quasiperpendicular shocks with $\nu < 3$, the relation between the energy and the pressure becomes more stiff; that is, for a given energy density that is absorbed in the ions downstream of the shock, the ion pressure is higher in the anisotropic plasma than it is in the isotropic one, so the pressure balance requires lower magnetic pressure. Thus, the magnetic compression is lower for an anisotropic plasma than for an isotropic distribution with the same upstream parameters. In quasiparallel shocks, the magnetic compression does not follow the density compression so closely, and the behavior can be different, as can be seen in Figure 8. While the density compression is higher in the isotropic case, the magnetic compression is larger for the anisotropic equation of state.

4. Conclusions

Observations at the Earth bow shock clearly show that downstream ion distributions are anisotropic well beyond the shock transition. The total pressure of the plasma is dominated by the ion pressure, so that proper boundary conditions, aka RH, should take into account this anisotropy. It is often expected that, at some distance behind the shock, the plasma will become isotropic, as a step toward reaching thermal equilibrium (note that equilibration of the temperatures among the species may not yet occur at the scale of isotropization). If this happens, and the approximations of planarity and stationarity are equally applicable in the anisotropic region and the isotropic region, with the same normal direction, the density should increase with the isotropization, so the plasma should experience additional deceleration along the shock normal. In quasiperpendicular shocks, the density increase is accompanied with a magnetic field increase, while in nearly parallel shocks, the magnetic field may decrease. These different density and magnetic compressions in isotropic and anisotropic regimes should be taken into account when applying theoretical RH to observations. At present, it is not

clear whether these changes can be observed in heliospheric observations, since isotropization may occur at scales that exceed the inhomogeneity scale. In any case, if isotropy is assumed in calculations or simulations, it is important not to compare the magnetic compression with that observed in a region where the plasma is still anisotropic. As found above, the differences may be substantial.

M. Gedalin was partially supported by NSF-BSF grant No. 2019744 and by the European Union's Horizon 2020 research and innovation program, under grant agreement No. 101004131 (SHARP). N.P. was supported, in part, by NSF-BSF award No. 2010450 and NASA grant No. 80NSSC18K1649. N.P. was additionally supported by the IBEX mission as part of NASA's Explorer program. V.R. was partially supported by NASA grant No. 80NSSC18K1649 and NSF-BSF award No. 2010144.

ORCID iDs

Michael Gedalin https://orcid.org/0000-0003-1236-4787
Nikolai V. Pogorelov https://orcid.org/0000-0002-6409-2392
Vadim Roytershteyn https://orcid.org/0000-0003-1745-7587

References

Abraham-Shrauner, B. 1967, JPlPh, 1, 379
Axford, W. I., Leer, E., & Skadron, G. 1977, in 15th Int. Cosmic Ray Conf., Vol 11 (Trieste: International Union of Pure and Applied Physics), 132
Balikhin, M., & Gedalin, M. 1994, GeoRL, 21, 841
Balikhin, M., Gedalin, M., & Petrukovich, A. 1993, PhRvL, 70, 1259
Balikhin, M. A., Pokhotelov, O. A., Walker, S. N., Boynton, R. J., & Beloff, N. 2010, GeoRL, 37, L05104
Bame, S., Mccomas, D., Barraclough, B., et al. 1992, A&AS, 92, 237
Bell, A. R. 1978, MNRAS, 182, 147
Blandford, R., & Eichler, D. 1987, PhR, 154, 1
de Hoffmann, F., & Teller, E. 1950, PhRv, 80, 692
Erkaev, N. V., Vogl, D. F., & Biernat, H. K. 2000, JPlPh, 64, 561
Farris, M. H., Russell, C. T., & Thomsen, M. F. 1993, JGR, 98, 15
Feldman, W., Bame, S., Gary, S., et al. 1982, PhRvL, 49, 199
Gedalin, M. 1997, SGeo, 18, 541
Gedalin, M. 2015, JPlPh, 81, 905810603
Gedalin, M. 2017, JGR, 122, 11857
Gedalin, M. 2019a, ApJ, 880, 140
Gedalin, M. 2019b, FrP, 7, 692
Gedalin, M. 2021, ApJ, 912, 82
Gedalin, M., & Balikhin, M. 2008, JPlPh, 74, 207
Gedalin, M., Friedman, Y., & Balikhin, M. 2015, PhPl, 22, 072301
Gedalin, M., Pogorelov, N. V., & Roytershteyn, V. 2020, ApJ, 889, 116
Gedalin, M., Pogorelov, N. V., & Roytershteyn, V. 2021, ApJ, 916, 57
Gedalin, M., & Zilbersher, D. 1995, GeoRL, 22, 3279
Génot, V. 2009, ASTRA, 5, 31
Giacalone, J. 2003, Plan. Sp. Sci., 51, 659
Hanson, E. L. M., Agapitov, O. V., Mozer, F. S., et al. 2019, GeoRL, 46, 2381
Hudson, P. 1970, Plan. Sp. Sci., 18, 1611
Jokipii, J. R. 1966, ApJ, 143, 961
Jokipii, J. R., Giacalone, J., & Kóta, J. 2007, Plan. Sp. Sci., 55, 2267
Jones, F. 1994, ApJS, 90, 561
Kennel, C. F. 1988, JGR, 93, 8545
Krasnosselskikh, V., Balikhin, M., Gedalin, M., & Lembège, B. 1995, AdSpR, 15, 239
Krymskii, G. F. 1977, Sov. Phys, Dokl., 22, 327
Li, X., Lewis, H. R., LaBelle, J., Phan, T. D., & Treumann, R. A. 1995, GeoRL, 22, 667
Lynn, Y. M. 1967, PhFl, 10, 2278
Lyu, L. H., & Kan, J. R. 1986, JGR, 91, 6771
Pollock, C., Moore, T., Jacques, A., et al. 2016, SSRv, 199, 331
Russell, C. T., Anderson, B. J., Baumjohann, W., et al. 2016, SSRv, 199, 189
Sagdeev, R. Z. 1966, Rev. Plas. Phys., 4, 23
Savoini, P., Lembege, B., Krasnosselskhik, V., et al. 2005, AnGeo, 23, 3685
Schwartz, S. J., Henley, E., Mitchell, J., & Krasnoselskikh, V. 2011, PhRvL, 107, 215002
Schwartz, S. J., Thomsen, M. F., Bame, S. J., & Stansberry, J. 1988, JGR, 93, 12923
Sckopke, N., Paschmann, G., Bame, S. J., Gosling, J. T., & Russell, C. T. 1983, JGR, 88, 6121
Sckopke, N., Paschmann, G., Brinca, A. L., Carlson, C. W., & Luehr, H. 1990, JGR, 95, 6337
Sonnerup, B. U. Ö 1969, JGR, 74, 1301
Thomsen, M., Stansberry, J., Bame, S., & Gosling, J. 1987, JGR, 92, 10119
Thomsen, M. F., Gosling, J. T., Bame, S. J., & Mellott, M. M. 1985, JGR, 90, 137
Tokar, R., Aldrich, C., Forslund, D., & Quest, K. 1986, PhRvL, 36, 1059
Toptyghin, I. N. 1980, SSRv, 26, 157
Vink, J. 2004, AdSpR, 33, 356
Vogl, D. F., Biernat, H. K., Erkaev, N. V., Farrugia, C. J., & Mühlbachler, S. 2001, NPGeo, 8, 167
Vogl, D. F., Langmayr, D., Erkaev, N. V., & Biernat, H. K. 2003, Plan. Sp. Sci., 51, 715